Chinese Journal of Aeronautics 25 (2012) 430-436

Contents lists available at ScienceDirect

Chinese Journal of Aeronautics

journal homepage: www.elsevier.com/locate/cja

Magnetometer Compensation Scheme and Experimental Results on ZDPS-1A Pico-satellite

HAN Ke, WANG Hao*, XIANG Tian, JIN Zhonghe

Department of Information Science and Electronic Engineering, Zhejiang University, Hangzhou 310027, China

Received 4 May 2011; revised 14 July 2011; accepted 23 September 2011

Abstract

In a pico-satellite with small volume, measurements from on-board three-axis magnetometer (TAM) are not accurate, as it can be easily disturbed by other electronic systems. To improve its accuracy, a scheme of compensation methods is introduced in this article. The scheme is based on an improved measurement model of pico-satellite TAM, and it mainly consists of three steps. First, in satellite design stage, several techniques are recommended to simplify the afterwards compensations. Then after satellite assembly, TAM ground tests and pre-launch calibration with least-square batch filter are introduced to improve magnetometer performance. At the end, a post-launch calibration with unscented Kalman filter (UKF) is implemented with in-orbit data. The compensation scheme is used in the development of Chinese pico-satellite ZDPS-1A made by Zhejiang University. Results show that with the introduced compensation scheme, the maximum error of ZDPS-1A TAM can be reduced from 80 mG to 6 mG (1 G=10^{-4} T).

Keywords: pico-satellite; magnetometers; calibration; least-square filter; Kalman filter

1. Introduction

By September 2009, more than 90 different pico- and nano-satellites have been launched into space [1]. The development of these light-weight satellites may significantly reduce space vehicle launch costs, as well as the manufacturing time. In practical applications, however, some problems rise. One of them is the low accuracy of on-board three-axis magnetometer (TAM). TAM can provide both direction and magnitude of the magnetic field, and it is generally a moderate accuracy sensor with the advantages of light-weight, reliable, low-power requirements and no moving parts [2]. However, there is one fatal disadvantage in TAM, that its measurement could be disturbed by any operating electronic systems. In pico- and nano-satellites, because of the small volume, there is no way inside the satellite body to keep a distance between TAM and other electronic systems. Deploying the TAM outside the satellite body might be an option [3], but it raises another problem in thermal control. The operating temperature outside the satellite body should be properly controlled, otherwise the reliability and lifetime of both TAM and deployed equipment cannot be guaranteed.

TAM is installed inside in many pico-satellites [4-5]. This is a reliable and easy way to install magnetometer on a satellite. However, the measurement disturbance cannot be ignored and should be compensated. Techniques on TAM compensation have been reported in recent researches [6-11]. These compensation methods mainly focus on the calibration of a number of factors, including biases, scale factors and nonorthogonality corrections, and good results have been achieved by testing with data from traditional satellites. However, for satellite with small volume, especially for pico-satellite, compensation method slightly differs.

*Corresponding author. Tel.: +86-571-87952151.
E-mail address: roger@zju.edu.cn
Foundation items: Program for New Century Excellent Talents in University (NCET-06-0514); China Postdoctoral Science Foundation (20081458, 20080431306)

1000-9361
doi: 10.1016/S1000-9361(11)60407-X

The bias, which is always assumed as constant in traditional satellites, is variable in pico-satellite. Because the distance between TAM and electronic systems is extremely short, any status changes, such as subsystem on/off switch, or solar panel current variation, could affect TAM's measurements. This complicates the problem and makes the current algorithm inadequate. To deal with it, modification is required.

In this study, a scheme of three-axis magnetometer compensation is introduced to deal with all these problems. The scheme is based on an improved measurement model of pico-satellite TAM, and it is involved in all stages of satellite development. In this article, the suggested scheme is implemented and verified with real data from a Chinese pico-satellite ZDPS-1A, made by Zhejiang University. With ground test and in-orbit data simulation, results show that, with all these calibration methods, the accuracy of ZDPS-1A on-board TAM can be guaranteed within 6 mG (1 G=10^{-4} T).

2. Pico-satellite Magnetometer Model

2.1. Design scheme of ZDPS-1A pico-satellite

In this research, a specific pico-satellite ZDPS-1A is studied. The shape of the satellite is like a cube, with four extended antennas. On all six faces of the cube, solar panels are installed in order to provide sufficient power. Inside the cube, battery and attitude control devices, along with satellite electronic systems are implemented. Satellite electronic systems consist of six printed circuit boards (PCBs); they are all fixed on a U-shaped frame. Between the inside system and the outside framework, some insulating materials are filled to perform passive thermal control.

A simplified design scheme of the satellite is provided in Fig. 1. The size of the cubic body is 15 cm×15 cm×15 cm, and the weight is about 3.5 kg. Obviously, it is very crowded inside the satellite. This is typical for small satellites, especially for pico- and nano-satellites. Generally, it may not create serious problems, as most on-board devices barely affect others. However, there is one device that is so sensitive that all electronic systems can affect its output, the three-axis magnetometer. In Fig. 1, magnetometer is installed on the sixth PCB, close to $+X$ and $+Z$ faces.

2.2. Measurement model of on-board magnetometer

For traditional satellites, measurement model for the on-board TAM can be written as [9]

$$\boldsymbol{B}_k = (\boldsymbol{I}_{3\times3} + \boldsymbol{D})^{-1}(\boldsymbol{O}^{\mathrm{T}}\boldsymbol{A}_k\boldsymbol{H}_k + \boldsymbol{b} + \boldsymbol{\varepsilon}_k) \quad (1)$$

where $\boldsymbol{B}_k$ is the measurement of the magnetic field by magnetometer at time k, $\boldsymbol{H}_k$ the corresponding value of the geomagnetic field with respect to an Earth-fixed coordinate system, $\boldsymbol{A}_k$ an attitude matrix of the magnetometer with respect to the Earth-fixed coordinates, $\boldsymbol{D}$ a symmetric matrix of scale factors (the diagonal elements) and non-orthogonality corrections (the off-diagonal elements), $\boldsymbol{O}$ an orthogonal matrix, $\boldsymbol{b}$ a bias vector, and $\boldsymbol{\varepsilon}_k$ the measurement noise vector that is assumed to be a zero-mean Gaussian process with covariance $\boldsymbol{I}_{3\times3}\sigma_{\mathrm{B}}^2$.

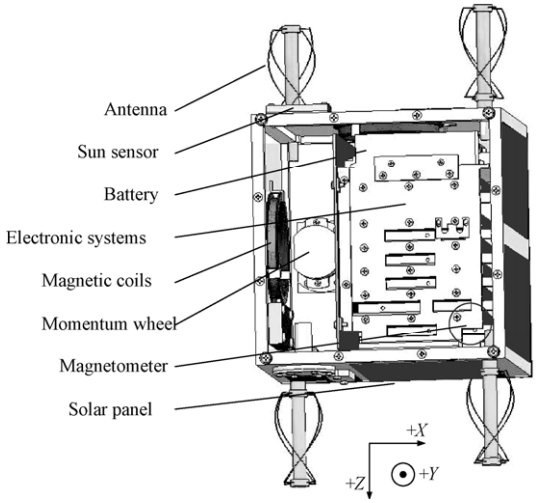

Fig. 1 Design scheme of ZDPS-1A pico-satellite.

In traditional satellites, as there is much more design margin in space allocation, the operation environment of magnetometer can be relatively clean. Therefore, only the static measurement bias is considered in measurement model. For pico-satellite, however, the dynamic measurement bias, which is caused by components with large current variations, should also be considered. A measurement model for pico-satellite on-board TAM can be written as

$$\boldsymbol{B}_k = (\boldsymbol{I}_{3\times3} + \boldsymbol{D})^{-1}(\boldsymbol{O}^{\mathrm{T}}\boldsymbol{A}_k\boldsymbol{H}_k + \boldsymbol{b} + \boldsymbol{C}\boldsymbol{I}_k + \boldsymbol{\varepsilon}_k) \quad (2)$$

Different from Eq. (1), a new term $\boldsymbol{C}\boldsymbol{I}_k$ is added to represent the dynamic measurement bias. $\boldsymbol{I}_k$ is a vector of operating current of different on-board components, and $\boldsymbol{C}$ the coefficient matrix which transforms the electronic current into magnetic disturbance. As the distance to magnetometer for all components is constant, according to Biot-Savart law, in this case, the induced magnetic field is proportional to electronic current. Therefore, every element in coefficient matrix $\boldsymbol{C}$ is constant.

2.3. Basic techniques in design stage

To compensate the TAM, matrices $\boldsymbol{D}$, $\boldsymbol{C}$, and vector $\boldsymbol{b}$ should all be estimated, and this can only be done after the final assembly of the satellite. To make the compensation procedure easier, however, several techniques are recommended in the design stage.

First, it is desirable to avoid using ferro- and paramagnetic materials such as iron and nickel, as there is a risk of magnetization of these materials. This is the same technique used in the cleanliness of residual magnetism [12]. As the environment keeps changing during manufacturing process of the satellite, the mag-

netization of these materials is unstable and unpredictable. This means unstable and unpredictable bias to magnetometer, which is very difficult to model and compensate.

Second, keeping positive and negative current wire as close as possible is recommended, as magnetic field has a direct relation to the enclosed current loop area. Smaller loop area means smaller induced field. This is especially important in the distribution of solar cell lead wires, because current through these wires is variable and changes extensively during daylight hours.

Third, for control devices with variable large current, such as magnetic coils, time division for its usage with the magnetometer is required; therefore the induced field of these devices can be eliminated. For picosatellite in this study, the control period is selected as 1 s, with 0.25 s for sensor data measurements, and 0.75 s for control torque output.

3. Ground Test and Pre-launch Calibration

3.1. Magnetometer bias test

Before ZDPS-1A assembly, all magnetometers were tested for their main characteristics: the scale factor, range, temperature effect, etc. The best sensor was selected to be the on-board one. After final assembly, the pico-satellite was sent to Zero Magnetic Field Laboratory of China Aerospace Science and Technology Corporation (CASC) for residual magnetism as well as magnetometer measurement tests. From these tests, static bias vector $\boldsymbol{b}_{\text{sta}}$ and dynamic bias vector $\boldsymbol{b}_{\text{dyn}}$ can be acquired. Table 1 shows the result.

In zero magnetic environments, the static bias vector $\boldsymbol{b}_{\text{sta}}$ of the magnetometer can be read directly from its output; and the dynamic bias vector $\boldsymbol{b}_{\text{dyn}}$ can be calculated from the difference of its measurements before and after satellite status changes. Referring to Eq. (2), there is

$$\boldsymbol{b}_{\text{sta}} = (\boldsymbol{I}_{3\times3} + \boldsymbol{D})^{-1}\boldsymbol{b} \tag{3a}$$

$$\boldsymbol{b}_{\text{dyn}} = (\boldsymbol{I}_{3\times3} + \boldsymbol{D})^{-1}\boldsymbol{C}\boldsymbol{I}_k \tag{3b}$$

Satellite status changes include telemetry tracking and command (TTC) A/B switch, on-board computer (OBC) A/B switch, sensor II (secondary in importance) on/off, and payload on/off. From Table 1, it is obvious that static bias $\boldsymbol{b}_{\text{sta}}$ has a large value, while the dynamic bias $\boldsymbol{b}_{\text{dyn}}$ is almost negligible. Because the magnetometer is installed closely to satellite electronic system, and there are also some magnetic chips for residual magnetism compensation inside satellite body, the static bias $\boldsymbol{b}_{\text{sta}}$ is large. Because the electronic current of OBC, sensor II and payload is relatively small (about 50 mA), its induced field is weak to magnetometer. For TTC board, although its current is about 400 mA, its distance to magnetometer is the largest among all PCBs. As a result, the disturbance from TTC A/B switch is also a small value.

Table 1 Magnetometer ground test results

mG

Bias vector		*X*	*Y*	*Z*
Static bias $\boldsymbol{b}_{\text{sta}}$		72.0	52.0	30.4
Dynamic bias $\boldsymbol{b}_{\text{dyn}}$	TTC A/B switch	0	−0.1	0.5
	OBC A/B switch	−0.2	0	0
	Sensor II on/off	0	−0.1	0.1
	Payload on/off	0	0	0.1

3.2. Solar panel influence test

Considering that the noise of the magnetometer is about 0.2 mG (1σ), the dynamic bias from subsystem status changes needs not to be compensated. However, there are still problems from the power supply system, specifically, the electronic current of solar panels. As said before, during daylight hours, solar panel current changes extensively; and because there are solar cells installed on all faces of satellite body, there is no way to avoid the disturbance. Wire distribution technique introduced in Section 2.3 can decrease the effect, but as the current is not small (more than 1 A), the effect cannot be eliminated.

A test was implemented to find out the influence of solar panels. During the test, satellite was placed on ground in sunlight, with a box covering it. One set of measurement data was read from wireless communication, and after that, the box was removed. Then, the other set of data was read, and the difference of two sets is the information of solar panel influence. This procedure was repeated dozens of times for different satellite orientation, and Fig. 2 shows the test results. The measured magnetometer bias $\boldsymbol{b}_{\text{test}}$ is shown in

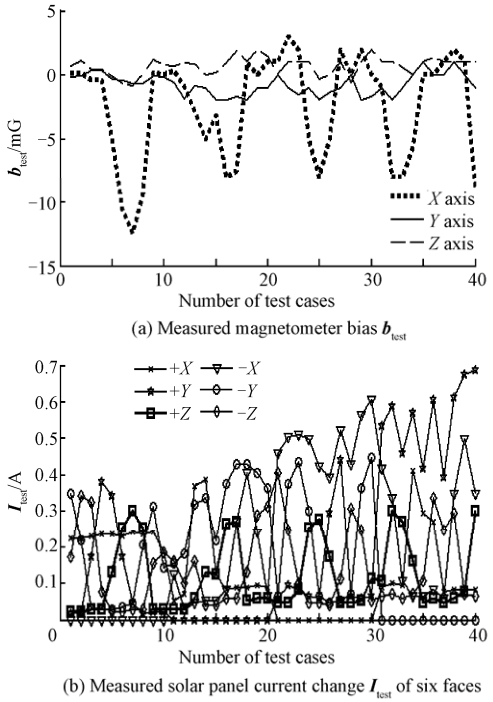

(a) Measured magnetometer bias $\boldsymbol{b}_{\text{test}}$

(b) Measured solar panel current change $\boldsymbol{I}_{\text{test}}$ of six faces

Fig. 2 Test results of the influence of solar panels.

Fig.2(a), and the corresponding solar panel current change $\boldsymbol{I}_{\text{test}}$ is shown in Fig. 2(b). From Fig. 2(a), it is very clear that the disturbance of X axis measurements is the heaviest. From Fig. 2(b), we see that the current of $+Z$ panel has a similar pattern with X axis magnetometer bias, which means that the influence from $+Z$ solar panel is the most significant. This phenomenon can be explained by magnetometer installation and solar cell lead wire distribution. Referring to Fig. 1, magnetometer is installed near $+Z$ and $+X$ faces. The distribution of lead wires in $+Z$ solar panel assembled right under the magnetometer, while distribution of wires in $+X$ solar panel assembled near $-Z$ panel. This is why $+X$ solar current has less significant effect than $-Z$ solar current on magnetometer.

3.3. Least-square batch filter

Compared with dynamic bias from subsystem status changes, the influence from solar panels is much larger, and it cannot be ignored. For cases without sunlight (k=T0), the measurement model of magnetometer can be written as

$$\boldsymbol{B}_{\text{T0}} = (\boldsymbol{I}_{3\times3} + \boldsymbol{D})^{-1}(\boldsymbol{O}^{\text{T}}\boldsymbol{A}_{\text{T0}}\boldsymbol{H}_{\text{T0}} + \boldsymbol{b} + \boldsymbol{\varepsilon}_{\text{T0}}) \quad (4)$$

For cases with sunlight (k=T1), the model is written as

$$\boldsymbol{B}_{\text{T1}} = (\boldsymbol{I}_{3\times3} + \boldsymbol{D})^{-1}(\boldsymbol{O}^{\text{T}}\boldsymbol{A}_{\text{T1}}\boldsymbol{H}_{\text{T1}} + \boldsymbol{b} + \boldsymbol{C}_{3\times6}\boldsymbol{I}_{\text{ST1}} + \boldsymbol{\varepsilon}_{\text{T1}}) \quad (5)$$

where $\boldsymbol{C}_{3\times6}$ is a coefficient matrix, and $\boldsymbol{I}_{Sk}$ (k=T1) the current vector of six solar panels, which can be written as

$$\boldsymbol{I}_{Sk} = \boldsymbol{I}_{\text{test}k} - \boldsymbol{e}_{Sk} \quad (6)$$

where $\boldsymbol{I}_{\text{test}k}$ is the measured current vector of six solar panels, and $\boldsymbol{e}_{Sk}$ the measurement noise vector which can be assumed to be a zero-mean Gaussian process with covariance $\boldsymbol{I}_{6\times6}\sigma_{\text{S}}^2$.

In both T0 and T1 cases, as satellite position and orientation do not change, the geomagnetic field $\boldsymbol{H}$ and attitude matrix $\boldsymbol{A}$ remain unchanged. Therefore, minus Eq. (5) with Eq. (4) on both sides, we get

$$\boldsymbol{b}_{\text{test T}} = \boldsymbol{B}_{\text{T1}} - \boldsymbol{B}_{\text{T0}} = (\boldsymbol{I}_{3\times3} + \boldsymbol{D})^{-1}[\boldsymbol{C}_{3\times6}(\boldsymbol{I}_{\text{testT1}} - \boldsymbol{e}_{\text{ST1}}) + \boldsymbol{\varepsilon}_{\text{T1}} - \boldsymbol{\varepsilon}_{\text{T0}}] \quad (7)$$

Equation (7) can be further written as

$$\boldsymbol{b}_{\text{test}k} = \boldsymbol{P}\boldsymbol{I}_{\text{test}k} - \boldsymbol{P}\boldsymbol{e}_{Sk} + (\boldsymbol{I}_{3\times3} + \boldsymbol{D})^{-1}(\boldsymbol{\varepsilon}_{\text{T1}} - \boldsymbol{\varepsilon}_{\text{T0}}) \quad (8)$$

where

$$\boldsymbol{P} = (\boldsymbol{I}_{3\times3} + \boldsymbol{D})^{-1}\boldsymbol{C}_{3\times6} \quad (9)$$

In Eq. (9), $\boldsymbol{D}$ and $\boldsymbol{C}_{3\times6}$ are unknown. To estimate them, a weighted least-square loss function is defined:

$$J(\boldsymbol{P}) = \sum_{k=1}^{N}(\boldsymbol{b}_{\text{test}k} - \boldsymbol{P}\boldsymbol{I}_{\text{test}k})^{\text{T}}\boldsymbol{W}(\boldsymbol{b}_{\text{test}k} - \boldsymbol{P}\boldsymbol{I}_{\text{test}k}) \quad (10)$$

where N is the number of test cases, and $\boldsymbol{W}$ the weight matrix of loss function, which is the inverse matrix of covariance of $(\boldsymbol{b}_{\text{test}k} - \boldsymbol{P}\boldsymbol{I}_{\text{test}k})$.

$$\boldsymbol{W} = \text{inv}\{E[(\boldsymbol{b}_{\text{test}k} - \boldsymbol{P}\boldsymbol{I}_{\text{test}k})(\boldsymbol{b}_{\text{test}k} - \boldsymbol{P}\boldsymbol{I}_{\text{test}k})^{\text{T}}]\} \quad (11)$$

Considering that $\boldsymbol{D}$ is always small, Eq. (11) can be further written as

$$\boldsymbol{W} = \text{inv}\{E[(-\boldsymbol{P}\boldsymbol{e}_{Sk} + \boldsymbol{\varepsilon}_{k1} - \boldsymbol{\varepsilon}_{k0})\cdot (-\boldsymbol{P}\boldsymbol{e}_{Sk} + \boldsymbol{\varepsilon}_{\text{T1}} - \boldsymbol{\varepsilon}_{\text{T0}})^{\text{T}}]\} = \text{inv}(\boldsymbol{P}\boldsymbol{P}^{\text{T}}\sigma_{\text{S}}^2 + 2\boldsymbol{I}_{3\times3}\sigma_{\text{B}}^2) \quad (12)$$

With Eq. (10) and Eq. (12), a nonlinear batch least-square filter can be implemented according to the Levenberg-Marquardt method [13-14]. Specifically, in practical applications, using the "solve" function in MATLAB with the option "optimset ("Algorithm", "levenberg-marquardt")" will be enough to solve the problem.

3.4. Pre-launch calibration

For solar panel influence test in Section 3.2, the covariance of magnetic field measurements σ_{B}^2 is (0.2 mG)^2, and the covariance of panel current measurements σ_{S}^2 is (0.01 A)^2. By using the batch filter introduced in Section 3.3, coefficient matrix $\boldsymbol{P}$ can be estimated. Table 2 shows the results

Table 2 Estimation results of coefficient matrix $\boldsymbol{P}$

mG/A

Solar panel	Magnetometer axis		
	X	Y	Z
$+X$	−6.315	1.707	−3.029
$-X$	2.064	−0.394	−1.640
$+Y$	4.701	−0.125	3.155
$-Y$	6.026	−2.982	5.068
$+Z$	−37.748	−3.960	−1.257
$-Z$	2.786	0.833	0.872

Notice that −37.748 mG/A is much larger than any other data in Table 2, which means that the disturbance in X axis from $+Z$ solar panel is the heaviest. This, again, explains the phenomenon that the current of $+Z$ panel has a similar pattern with X axis magnetometer bias in Fig. 2. Using matrix $\boldsymbol{P}$, the calibrated measurement bias $\boldsymbol{b}_{\text{cal}}$ can be calculated as $(\boldsymbol{b}_{\text{test}} - \boldsymbol{P}\boldsymbol{I}_{\text{test}})$. Figure 3 shows the calibrated measurement error $(\boldsymbol{b}_{\text{cal}} - \boldsymbol{b}_{\text{T0}})$ of the 40 cases in Fig. 2.

Compared with Fig. 2, magnetometer measurement error in Fig. 3 is significantly reduced, from a maximum of 13 mG to about 1.5 mG. This result is acceptable, and it demonstrates the effectiveness of the calibration method. However, it is still not good enough. The main source of inaccuracy is the measurement of solar panels current. In the initial design of the satellite, current data of solar panels are only used for satellite status monitor, therefore the measurement circuit is simply designed and the raw data are provided without any filtering process. As a result, the covariance σ_{s}^2 of solar panel current is too high, and it should be improved in further developments.

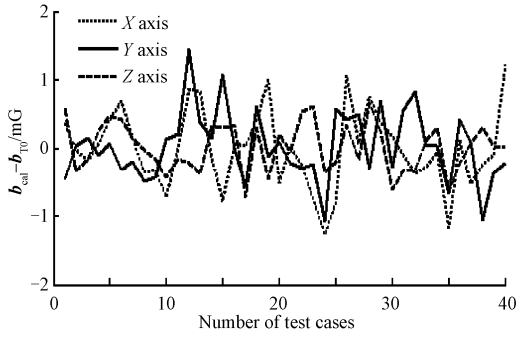

Fig. 3 Calibrated magnetometer measurement error ($\boldsymbol{b}_{\text{cal}} - \boldsymbol{b}_{\text{T0}}$).

4. Post-launch Calibration and Simulation

4.1. Unscented Kalman calibration filter

After ground test and pre-launch calibration, coefficient matrix $\boldsymbol{P}$ can be acquired, then Eq. (2) can be written as

$$\boldsymbol{B}_k = (\boldsymbol{I}_{3\times3} + \boldsymbol{D})^{-1}(\boldsymbol{O}^{\mathrm{T}}\boldsymbol{A}_k\boldsymbol{H}_k + \boldsymbol{b} + \boldsymbol{\varepsilon}_k) + \boldsymbol{P}(\boldsymbol{I}_k - \boldsymbol{e}_{\text{Sk}}) \tag{13}$$

In Eq. (13), matrix $\boldsymbol{D}$ and vector $\boldsymbol{b}$ are two unknown parameters, which are the target of post-launch calibration. Adopting a similar way to real-time attitude-independent three-axis magnetometer calibration [8], define a measurement function as

$$\begin{aligned} h(\boldsymbol{x}) = \left\|\boldsymbol{B}_k - \boldsymbol{P}\boldsymbol{I}_k\right\|^2 - \left\|\boldsymbol{H}_k\right\|^2 = \\ -\boldsymbol{N}_k^{\mathrm{T}}(2\boldsymbol{D} + \boldsymbol{D}^2)\boldsymbol{N}_k + \\ 2\boldsymbol{N}_k^{\mathrm{T}}(\boldsymbol{I}_{3\times3} + \boldsymbol{D})\boldsymbol{b} - \left\|\boldsymbol{b}\right\|^2 + v_k \end{aligned} \tag{14}$$

where

$$\boldsymbol{N}_k = \boldsymbol{B}_k - \boldsymbol{P}\boldsymbol{I}_k \tag{15}$$

$\boldsymbol{x}$ is the state vector with nine constant elements,

$$\boldsymbol{x} = \begin{bmatrix} \boldsymbol{b}^{\mathrm{T}} & D_{11} & D_{22} & D_{33} & D_{12} & D_{13} & D_{23} \end{bmatrix}^{\mathrm{T}} \tag{16}$$

There is a reason that the coefficient matrix $\boldsymbol{P}$ is not included in the state vector. Because there is too many elements in $\boldsymbol{P}$ (18 in this case), the filter which estimates $\boldsymbol{P}$ may not operate in real time. For bias vector $\boldsymbol{b}$, however, although a static bias vector $\boldsymbol{b}_{\text{sta}}$ has been acquired in ground tests, estimation is still recommended for higher accuracy.

In Eq. (14), v_k is the noise and

$$\begin{aligned} v_k = 2[(\boldsymbol{I}_{3\times3} + \boldsymbol{D})\boldsymbol{N}_k - \boldsymbol{b}]^{\mathrm{T}}(\boldsymbol{\varepsilon}_k - \boldsymbol{C}\boldsymbol{e}_k) - \\ \left\|\boldsymbol{\varepsilon}_k\right\|^2 - \boldsymbol{e}_k^{\mathrm{T}}\boldsymbol{C}^{\mathrm{T}}\boldsymbol{C}\boldsymbol{e}_k - 2\boldsymbol{\varepsilon}_k^{\mathrm{T}}\boldsymbol{C}\boldsymbol{e}_k \end{aligned} \tag{17}$$

v_k is approximately Gaussian with the mean denoted by μ_k and variance denoted by σ_k^2, each given by

$$\mu_k \equiv E(v_k) = -3\sigma_{\text{B}}^2 - \text{tr}(\boldsymbol{C}^{\mathrm{T}}\boldsymbol{C})\sigma_{\text{S}}^2 \tag{18a}$$

$$\begin{aligned} \sigma_k \equiv E((v_k - \mu_k)^2) = \\ 4\sigma_{\text{B}}^2[(\boldsymbol{I}_{3\times3} + \boldsymbol{D})\boldsymbol{N}_k - \boldsymbol{b}]^{\mathrm{T}}[(\boldsymbol{I}_{3\times3} + \boldsymbol{D})\boldsymbol{N}_k - \boldsymbol{b}] + \\ 4\sigma_{\text{S}}^2[(\boldsymbol{I}_{3\times3} + \boldsymbol{D})\boldsymbol{N}_k - \boldsymbol{b}]^{\mathrm{T}}\boldsymbol{C}\boldsymbol{C}^{\mathrm{T}}[(\boldsymbol{I}_{3\times3} + \boldsymbol{D})\boldsymbol{N}_k - \boldsymbol{b}] + \\ 6\sigma_{\text{B}}^4 + 2\sigma_{\text{S}}^4\sum_{i,j=1}^{6}T_{i,j}^2 + 2\sigma_{\text{B}}^2\sigma_{\text{S}}^2\sum_{i=1}^{3}\sum_{j=1}^{6}C_{i,j}^2 \end{aligned} \tag{18b}$$

where $\boldsymbol{T} = \boldsymbol{C}^{\mathrm{T}}\boldsymbol{C}$, and $T_{i,j}$ is the i row, j column element of $\boldsymbol{T}$. With these equations, an unscented Kalman filter can be implemented. The filter is similar to that by the calibration algorithm introduced by Crassidis, et al. [8]. The only difference between two algorithms is the definition of measurement function and calculation of its covariance. The filtering processes of two algorithms are exactly the same. Therefore, in this paper, the implementation procedure of the unscented Kalman filter is not reported.

4.2. Post-launch calibration with in-orbit data

On September 22, 2010, two ZDPS-1A picosatellites were launched from Jiuquan Satellite Launch Center, China. Both satellites were built by Zhejiang University with the purpose of scientific research. Both satellites were put in a sun synchronous orbit with altitude of 645 km, and the local time of descending node of 09:00:00. Satellites' in-orbit data were received and stored by ground station after launch, and in this section, the data from the second ZDPS-1A pico-satellite's on-board magnetometer are used for analysis. Figure 4 shows the original measurement data from the TAM, and the start time of the figure is set at 00:00:00 September 22, 2010 UTC. B_{kx}, B_{ky} and B_{kz} are three axis components of $\boldsymbol{B}_k$. As the downlink of ZDPS-1A is not

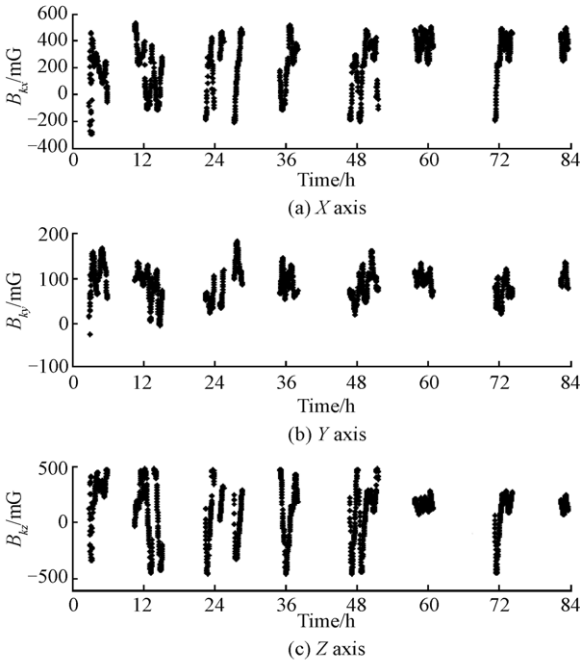

Fig. 4 In-orbit magnetometer data of ZDPS-1A.

high enough, very few data were collected. To analyze the effectiveness of post-launch calibration, separated data from more than three days are calculated in this simulation.

In simulation, UKF introduced in Section 4.1 is implemented. The initial value of the calibration filters is set as

$$\begin{cases} \boldsymbol{x}_0 = \boldsymbol{0}_{9\times1} \\ \boldsymbol{P}_0 = \begin{bmatrix} 500\boldsymbol{I}_{3\times3} & \boldsymbol{0}_{3\times6} \\ \boldsymbol{0}_{6\times3} & 0.001\boldsymbol{I}_{6\times6} \end{bmatrix} \end{cases} \tag{19}$$

And the variance of the measurement noise is set as

$$\begin{cases} \sigma_{\mathrm{S}} = 0.01\ \mathrm{A} \\ \sigma_{\mathrm{B}} = 0.2\ \mathrm{mG} \end{cases} \tag{20}$$

Figure 5 shows the simulation result of estimated bias $\boldsymbol{b}$. Within 400 filtering steps, filter converges to a steady state, and the final estimated value is about [78.87 62.02 35.47] mG, which is similar to the pre-launch static bias $\boldsymbol{b}_{\mathrm{sta}}$ in Table 1. Notice that the estimated bias of Y axis is not as steady as X and Z. This is because compared with two other axes, the Y axis data of the on-board TAM in Fig. 4 vary in a smaller range, which makes the filter need more measurements to complete its convergence.

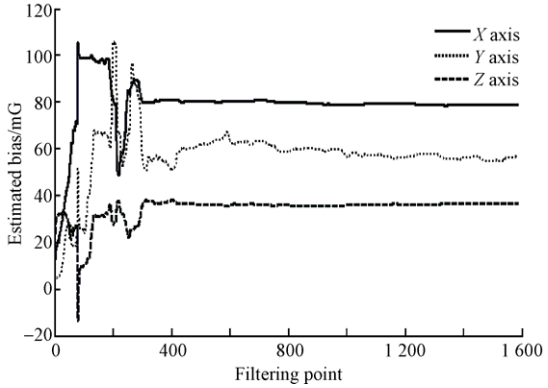

Fig. 5 Estimated bias $\boldsymbol{b}$ from the post-launch calibration filter.

Figure 6 shows the estimation curve of matrix $\boldsymbol{D}$. Only half of its elements are shown in the figure, as the other half just follow the same pattern. As shown in the figure, the filter converges to its steady state within 400 filtering steps, and the final value of [D_{11} D_{22} D_{33} D_{12} D_{13} D_{23}] is about [0.000 9 0.065 6 −0.003 8 0.002 5 0.002 4 0.037 1].

With post-launch calibration, the bias vector $\boldsymbol{b}$ as well as the symmetric matrix $\boldsymbol{D}$ are all estimated. Along with the pre-launch calibration coefficient matrix $\boldsymbol{P}$, the output of magnetometer can be re-calculated to achieve a higher accuracy. As the attitude of ZDPS-1A is not always precisely measured by on-board computer, in this article, the effectiveness of the magnetometer compensation is demonstrated by comparing the magnitude of TAM measurements. Figure 7 shows part of the comparison result. The ideal magnitude value is calculated by international geomagnetic reference field (IGRF) magnetic field model; the value without calibration is calculated from raw data in Fig. 5; the value with calibration is the result of the suggested method in this article. It is clear that the data after calibration largely overlap the data with ideal value. This means with the method of this article, the measurement accuracy of TAM can be significantly increased.

Figure 8 shows the error of TAM measurements. Corresponding to Fig. 7, the measurement error before calibration in Fig. 8 is the difference from the raw data to the ideal magnitude value; the error after calibration is the difference from the calibrated value to the ideal value.

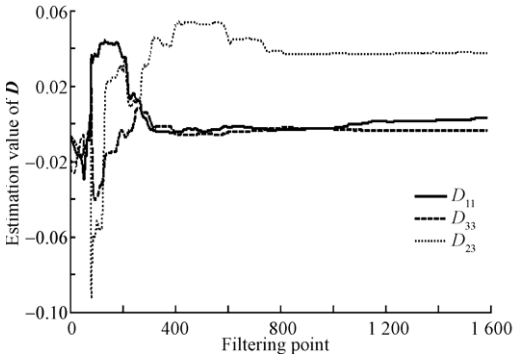

Fig. 6 Estimated $\boldsymbol{D}$ from the post-launch calibration filter.

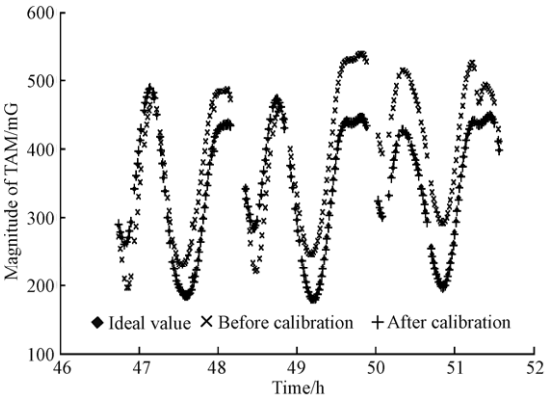

Fig. 7 Magnitude of TAM measurements before and after calibration.

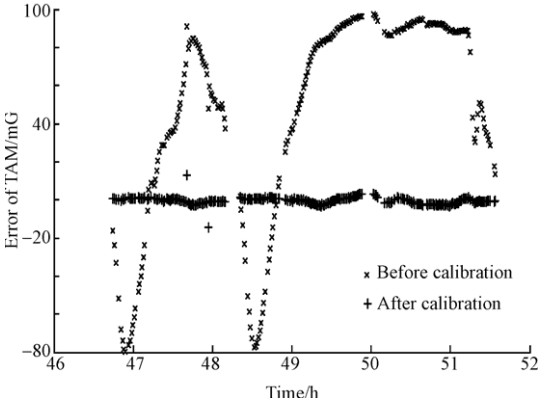

Fig. 8 Error of TAM measurements, before and after calibration.

It is obvious that the measurement error decreases significantly after calibration, which means the compensation scheme of on-board TAM is essential and effective. In Fig. 8, besides two large error points around 48 h (which might be caused by data transmitting error), most TAM error after calibration is within 6 mG. Computing with all data in Fig. 5, with the suggested compensation scheme, the mean value of on-board TAM error is about −0.5 mG, and the covariance about 2.3 mG.

5. Conclusions

In this article, a magnetometer compensation scheme for pico-satellite is proposed. The scheme mainly consists of three steps: design stage consideration to simplify the afterwards compensations, pre-launch calibration with a weighted least-square batch filter, and post-launch calibration with an unscented Kalman filter. Based on a Chinese pico-satellite ZDPS-1A made by Zhejiang University, the scheme is implemented and verified with real data. Result shows that with all these calibration methods, the accuracy of ZDPS-1A on-board TAM can be guaranteed within 6 mG. TAM error of this level already satisfies the requirement of low accuracy pico-satellite attitude control system. In ZDPS-1A project, with their on-board TAM, both satellites complete their in-orbit three-axis stabilization control test. The orientation accuracy of ZDPS-1A pico-satellites is approximately 5°.

References

[1] Bouwmeester J, Guo J. Survey of worldwide pico- and nanosatellite missions, distributions and subsystem technology. Acta Astronautica 2010; 67(7-8): 854-862.
[2] Han K, Wang H, Jin Z H. Magnetometer-only linear attitude estimation for bias momentum pico-satellite. Journal of Zhejiang University SCIENCE A 2010; 11(6): 455-464.
[3] Vega K, Auslander D, Pankow D. Design and modeling of an active attitude control system for CubeSat class satellites. AIAA-2009-5812, 2009.
[4] Scholz A, Ley W, Dachwald B, et al. Flight results of the COMPASS-1 picosatellite mission. Acta Astronautica 2010; 67(9-10): 1289-1298.
[5] Ashida H, Fujihashi K, Inagawa S, et al. Design of Tokyo Tech nano-satellite Cute-1.7+APD II and its operation. Acta Astronautica 2010; 66(9-10): 1412-1424.
[6] Alonso R, Shuster M D. Complete linear attitude-independent magnetometer calibration. Journal of the Astronautical Sciences 2002; 50(4): 477-490.
[7] Alonso R, Shuster M D. TWOSTEP: a fast robust algorithm for attitude-independent magnetometer-bias determination. Journal of the Astronautical Sciences 2002; 50(4): 433-451.
[8] Crassidis J L, Lai K L, Harman R R. Real-time attitude-independent three-axis magnetometer calibration. Journal of Guidance, Control, and Dynamics 2005; 28(1): 115-120.
[9] Kim Y V, Di Filippo K J, Ng A, et al. On the calibration of satellite on-board magnetometer, control and automation. Proceedings of 4th International Conference on Control and Automation. 2003; 947-951.
[10] Duan F, Liu J Y, Li R B, et al. Real-time attitude- independent sun-sensor/magnetometer calibration algorithm for micro-satellite. Proceedings of SPIE. 2005; 5985: 598548-1-598548-5.
[11] Huang L, Jing W X. Attitude-independent geomagnetic navigation using onboard complete three-axis magnetometer calibration. IEEE Aerospace Conference. 2008; 1-7.
[12] Stern T G, Delapp S. Techniques for magnetic cleanliness on spacecraft solar arrays. 2nd International Energy Conversion Engineering Conference. 2004.
[13] Levenberg K. A method for the solution of certain problems in least squares. Quarterly of Applied Mathematics 1944; 2: 164-168.
[14] Marquardt D W. An algorithm for least-squares estimation of nonlinear parameters. SIAM Journal on Applied Mathematics 1963; 11(2): 431-441.

Biographies:

HAN Ke received M.S. and Ph.D. degrees from Zhejiang University in 2006 and 2011. His main research interest lies in estimation, navigation and control of pico-satellite attitude determination and control system.
E-mail: zjuhank@gmail.com

WANG Hao received Ph.D. degree from Shanghai Jiaotong Unversity in 2007, and then became an associate professor at Zhejiang University. His main research interest lies in system design of pico-satellite attitude determination and control system.
E-mail: roger@zju.edu.cn